Lagrangian Actuator Model For Wind Turbine Wake Aerodynamics

Liu Weiqi[a,b], Shi Jian[a,*], Chen Hailong[b], Liu Hengxu[b], Lin Zi[c], Wang Lingling[b]

[a] *School of Automation Science and Electrical Engineering, Beihang University, Beijing 100191, China*
[b] *Yantai Research Institute and Graduate School, Harbin Engineering University, Yantai 264006, China*
[c] *Department of Naval Architecture, Ocean and Marine Engineering, University of Strathclyde, Glasgow SC015263, UK*

Abstract

As a continuation of authors' previous work, this work extends and hackles the numerical method for wind turbine wakes based on the vortex method, and proposes the Lagrangian actuator model (LAM) which is used for the representation of the wind turbine rotor under the Lagarangian framework. This paper provides two examples of the LAM, the Lagrangian actuator line (LAL) model and the Lagrangian actuator disc (LAD) model, and constructs matching numerical methods for wake predictions respectively. Those methods have high computation efficiency, and the results coincide with the wind tunnel test data well. Moreover, based on that, a vorticity description framework centered on vortex geometric structures is established to illustrate wind turbine wake phenomena and explore the wake evolution mechanism.

Keywords: Wind turbine Wake, Lagrangian framework, Actuator model, Vortex method

1. Introduction

With the large-scale development of wind farms, the problem of wake disturbance of wind turbines is becoming more prominent [1]. A wake is the downstream flow field disturbed by a wind turbine. One of its specific demonstrations is the velocity deficit that causes power loss of downstream wind turbines. It is estimated that the power loss caused by the wake effect accounts for 5%-20% of the total generating capacity at a large wind farm [2]. It is apparent that the wake effect among wind turbines plays an important role in the layout optimization and economic evaluation of a wind farm [3].

Typical wind turbine velocity profiles in a wind turbine wake are shown in Fig.1. There is an M-shape wake velocity profile close to the wind turbine (Zone A). Along the downstream distance, it gradually takes the shape of a "bell" like the Gaussian function, and finally recovers to the uniform inflow velocity profile (Zone B). The two zones are named as the near wake and the far wake, respectively [4, 5]. The distinction between them is on the basis of the complexity of the wake field: the near wake is strongly influenced by the wind turbine rotor, dominated by the pressure, and its velocity field is more complex; the far wake seldom retains rotor geometry and movement information and is controlled by the turbulence, where the velocity field is relatively simple [6]. However, until now, there has been no clear agreement on the dividing point between them. It is generally considered that the near wake covers the scope from the rotor to 1-3 times the rotor

*Co-first author, Corresponding author
Email address: shijian123@sina.com (Shi Jian)

diameter along the downstream distance [4], and far wake refers to the scope outside the scope of the near wake (some scholars tend to extend the near wake scope to the 5 times the rotor diameter[5]).

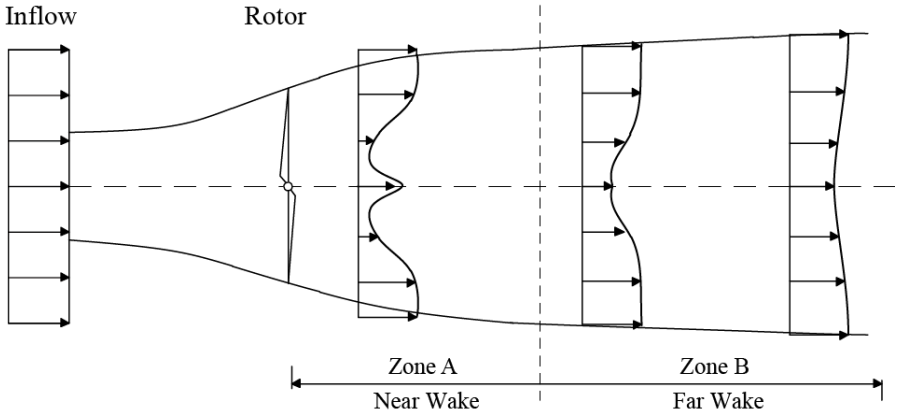

Figure 1: Velocity profiles in a wind turbine wake.

Currently there are two common approaches to forecast the wake velocity deficit, the analytical wake model method and the numerical method based on Computational Fluid Dynamics (CFD) [4].

The analytical wake model dates back to 1980s. It describes the distribution of the velocity deficit along the downstream distance in a wake, identifying the optimal distance among wind turbines in a wind farm. Under some phenomenological assumptions, the analytical wake model derives a simple semi-empirical formula based on conservation laws of momentum and mass. The model is super-fast and low-cost, but failed to consider fluid features and wake evolution processes. The first analytical wake model is the Jensen wake model, which is also called the top-hat wake model [7]. The model assumes that the wake region shows linear expansion along the flow direction, and the wake velocity distribution is even and in the shape of a top-hat. With a simple form and high efficiency, the Jensen model is widely applied in commercial software like WAsP, WindFarmer [8]. Since then, the Jensen model has been improved continuously in many aspects, among which the most important one lies in the revision of the velocity profile shape. Wind tunnel investigations and field observations show that the velocity profile in the far wake region takes the shape of the Gaussian function instead of the even distribution assumed in the Jensen model [9, 10]. Thus, long after that, the wake velocity profiles in analytical wake models take the shape of the Gaussian function or any other similar polynomial and trigonometric functions [11, 12]. Furthermore, considering the wind variation in the height direction, a 3D wake model is presented, which is more accurate and closer to the reality [13, 14, 15]. However, the model is has difficulty describing the flow field near the rotor. To this end, some studies have tried describing the velocity profiles in the near wake using two Gaussian functions [16]. Obviously, the complexity of the velocity field in this region is beyond the scope where the velocity profile can be described simply by a phenomenological model.

Generally, there are three methods to compute wind turbine wakes numerically, Direct Numerical Simulation (DNS) [17], Large Eddy Simulation (LES) [18, 19] and Reynolds Averaged Navier Stokes (RANS) [20]. DNS has a high cost in computation and therefore it is not commonly used in the simulation of wind turbine wakes. Compared with RANS, LES has an advantage in wake prediction because of its ability to handle turbulent flows dominated by large-scale structures and turbulent mixing [21]. Besides, some simplified algorithms

based on the general CFD technique have been proposed for the wake issue specially in order to reduce the computational cost [22, 23]. Two approaches to handling the wind turbine rotor exist, the actuator model approach, in which the rotor is represented by a body force with a simple geometry, and the direct approach, in which the presence of the rotor is taken into account by discretizing the actual rotor on a computational mesh [21]. According to the simplicity degree of the rotor from high to low, the actuator model can be further divided into the actuator disc (AD) model [24], the actuator line (AL) model [25] and the actuator surface (AS) model [26]. The greatest advantage of the actuator model lies in avoiding the displayed computation of the boundary layer, decreasing the model's complexity in geometry and the number of grids. In 1990, the AD model is first proposed [27]. It is applied to aerodynamic computation of vertical axis wind turbines coordinating with the CFD technology. It is then launched to horizontal axis wind turbines. Early this century, the AL model and the AS model are proposed respectively as the improvement of the AD model. Among them, the AL model is widely used in engineering because of its good precision and acceptable computation cost [28, 29, 30].

Based on the literature review above, two main methods exist for the wind turbine wake prediction, the analytical wake model method and the numerical method based on the CFD technology. The former is a typical phenomenological method with high efficiency, but it works only in a part of the wake. The latter, actually, is an application of the CFD technology in wind turbine wake predictions, and the actuator model is an important supplement for it. It computes and displays very detailed fluid field information in the whole wake with a high computation cost. In addition, neither method is helpful in simply understanding the wake issue.

In 2018, authors presented a new numerical wake model using the vortex method[31], according to the fact that there are distinct vortex structures in wind turbine wakes. The model works in the whole wake and has acceptable efficiency. As a continuation, this paper extends and hackles a systematic method for wind turbine wakes based on the vortex method under the Lagrangian framework, and proposes the Lagrangian actuator model to solve the difficulty of boundary conditions on the wind turbine rotor. Furthermore, based on the method, a vorticity description is established for wind turbine wakes to illustrate the wake phenomena and explore the wake evolution mechanism.

2. Lagrangian Actuator Model

The Lagrangian actuator model is so named because of its strong correlation with the generalized actuator model in CFD simulations under the Eulerian framework. To avoid misunderstanding, the actuator model used in the CFD technology is called the Eulerian actuator model in this paper. The wind turbine rotor is treated as a simple geometry pushing the surrounding flow field in the Eulerian actuator model or releasing vortices into the air in the Lagrangian actuator model.

2.1. Lagrangian Actuator Line Model

The Lagrangian actuator line (LAL) model treats the wind turbine rotor as a generator continuously releasing vortex lines into air. The releasing position and the vortex circulation can be identified through the

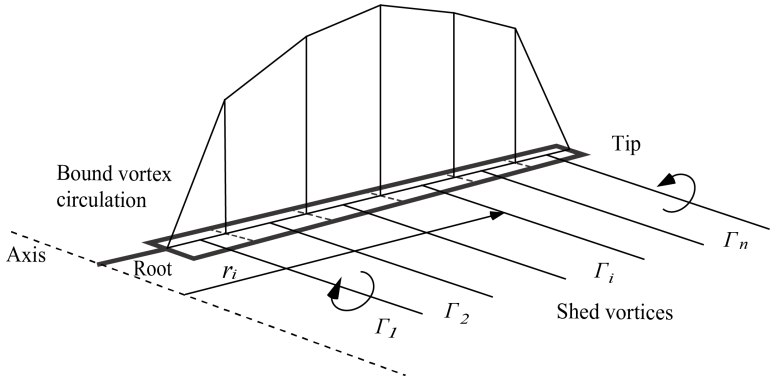

Figure 2: Shed vortices on a blade.

blade element momentum (BEM) theory. For each element on the blade, it is easy to obtain the unit length lift F_l and the relative velocity V_{rel} through the BEM theory, then the circulation of the bound vortex Γ_{bound} can be given as

$$\Gamma_{bound} = \frac{F_l}{\rho V_{rel}}, \tag{1}$$

where ρ is the air density. Ulteriorly, using the circulation conservation law, circulations of discrete shed vortices Γ_1,Γ_2,..., Γ_n can be obtained, as shown in Fig.2.

As known from experiments and numerical simulations, the vortices shed from a blade roll up to a tip vortex and a root vortex in a short downstream distance [32]. To calculate circulations and positions of roll-up vortices, assume that circulation and it's first, second, and third order moments are conserved in the roll-up process as

$$\Gamma_T \, r_T^k + \Gamma_R \, r_R^k = \sum_{i=1}^{n} \Gamma_i \, r_i^k, \tag{2}$$

where $k = 0, 1, 2, 3$. Γ_T, Γ_R, r_T and r_R are circulations and radial distances of the tip vortex and the root vortex respectively. In this way, shed vorticities on a blade are simplified into a tip vortex and a root vortex with equal strength (absolute value).

According to the above process, the transformation of the wind turbine rotor to the Lagrangian actuator line can be completed, as shown in Fig.3. For a wind turbine with a number of blades B, the rotor will be treated as a vortex line generator with 2B release positions, which are located near the root and the tip of each blade respectively. During the blade rotation, the generator continuously releases vortices into the flow field, gradually forming 2B helix-like vortex lines in the wake.

2.2. Lagrangian Actuator Disc Model

The Lagrangian actuator line model can be further simplified: the vortex generator intermittently releases vortex rings into the flow field instead of continuously releasing vortex lines as shown in Fig.4. Those vortex rings can be divided into two groups with exactly opposite circulations, representing the tip vortex and the root vortex respectively. This simplified model is called the Lagrangian actuator disc (LAD) model as the rotor in this model is like a disc with a hole, slapping the fluid intermittently, causing its inner and outer edges

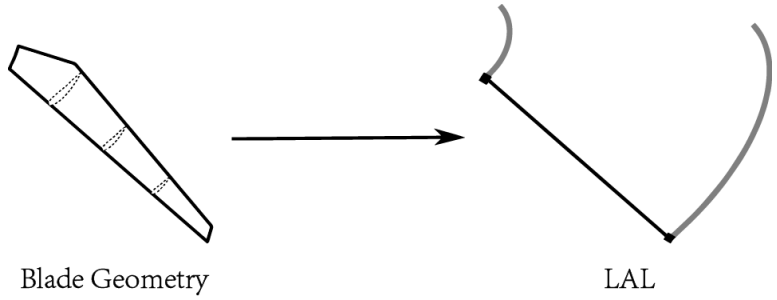

Figure 3: The Lagrangian actuator line model.

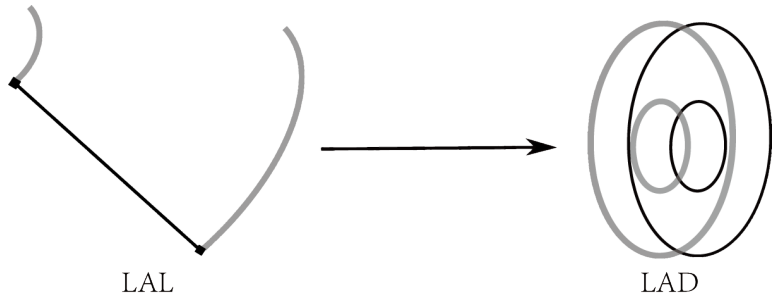

Figure 4: The Lagrangian actuator disc model.

to generate vortex rings periodically. Compared with the LAL model, the LAD model can greatly improve the computation efficiency.

The following content discusses the way to identify the parameter configuration of the vortex ring generator. Obviously, the radius of the vortex ring should be the same as that of the helical vortex line, r_T for the tip vortex, r_R for the root vortex. There are then two parameters to be discussed for the tip vortex ring and the root vortex ring, the circulation Γ_S and the releasing interval T_S between two continuous vortex rings. Here, consider a simple condition: in the uniform and stable background flow field, ignoring the interaction between vortices, a vortex line generator releases a standard helical vortex line, while a vortex ring generator releases an equidistant sequence of vortex rings. Then the discussion is simplified into that with what parameter configuration can a unidirectional equidistant sequence of vortex rings be as close as possible to a semi-infinite length helical vortex line in terms of the induced velocity?

For simplicity, the far field is first considered. In this case, take induced velocities of an infinite helical vortex line and of a bidirectional vortex ring sequence as the comparative objects. For an infinite length helical vortex line with the circulation of Γ, the parameter equation of its geometry is

$$\begin{cases} x = \frac{h\theta}{2\pi}, \\ y = R\cos(\theta - \varphi), \\ z = R\sin(\theta - \varphi), \end{cases} \tag{3}$$

where h is the helix pitch, R is the helix radius, $\varphi \in [0, 2\pi]$ represents the generality of the helix, $\theta \in (-\infty, +\infty)$.

On the above formula, integrate the Biot-Savart law

$$\mathrm{d}\boldsymbol{v} = -\frac{\Gamma}{4\pi}\frac{\boldsymbol{r}\times\mathrm{d}\boldsymbol{l}}{|\boldsymbol{r}|^3}, \tag{4}$$

then it is easy to get the induced velocity in the x direction (also the wind direction) v_x of the coordinate origin

$$v_x = \frac{\Gamma}{h}. \tag{5}$$

On the other hand, for the bidirectional sequence of vortex rings with the circulation of Γ_S, the parameter equation is

$$\begin{cases} x = (n+\varepsilon)h_S, \\ y = R\cos\theta, \\ z = R\sin\theta, \end{cases} \tag{6}$$

where $n = -\infty, \cdots, -1, 0, 1, \cdots, +\infty$, $\theta \in [0, 2\pi)$, h_S is the interval between adjacent vortex rings, $\varepsilon \in [0, 1)$ represents the generality of the sequence considering the periodicity. It is easy to see that the induced velocity of the vortex ring sequence in x direction of the coordinate origin is the sum of infinite series

$$v_{S,x} = \frac{\Gamma_S}{2R}\sum_{n=-\infty}^{+\infty}\left(1+\frac{h_S^2}{R^2}(n+\varepsilon)^2\right)^{-\frac{3}{2}}. \tag{7}$$

Apparently, the sum of infinite series is convergent. Let

$$S = \sum_{n=-\infty}^{+\infty}\left(1+\frac{h_S^2}{R^2}(n+\varepsilon)^2\right)^{-\frac{3}{2}}, \tag{8}$$

$$v_{S,x} = \frac{\Gamma_S}{2R}S. \tag{9}$$

Note that

$$\sum_{n=-\infty}^{+\infty}\left(1+\frac{h_S^2}{R^2}(n+\varepsilon)^2\right)^{-\frac{3}{2}} = \sum_{n=-\infty}^{+\infty}\left(1+\frac{h_S^2}{R^2}(n+1-\varepsilon)^2\right)^{-\frac{3}{2}}. \tag{10}$$

The symmetry means that the range of ε can be narrowed to $[0, 0.5]$. We hope $S \propto R/h_S$, which will make v_x and $v_{S,x}$ similar in form. Actually, it will be satisfied as long as R/h_S is limited within a certain scope, as shown in Fig.5.

It is easy to get that when

$$\frac{h_S}{R} \le 1, \tag{11}$$

no matter what value the ε is,

$$S \approx \frac{2R}{h_S}. \tag{12}$$

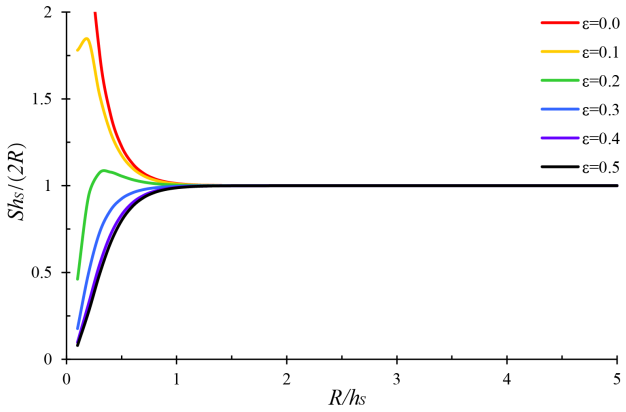

Figure 5: The relationship between $Sh_S/(2R)$ and R/h_S.

Then

$$v_{S,x} = \frac{\Gamma_S}{2R} S \approx \frac{\Gamma_S}{h_S}. \tag{13}$$

Let $v_x = v_{S,x}$, then

$$\frac{\Gamma}{h} = \frac{\Gamma_S}{h_S}. \tag{14}$$

Now, we get two constraints, Eq.11 and Eq.14, regarding the sequence of vortex rings.

Following a similar process as above descriptions, we can explore the near wake region to look for possible and more strict constraints. The parameter equation of a semi-infinite length helical vortex line is also the Eq.3. For convenience, let $\alpha = \theta - \varphi$, then

$$\begin{cases} x = \frac{h(\alpha+\varphi)}{2\pi}, \\ y = R\cos\alpha, \\ z = R\sin\alpha, \end{cases} \tag{15}$$

where $\alpha \in (-\varphi, +\infty)$. By integrating the Biot-Savart law, it is easy to get the induced velocity in the x direction v_x of the semi-infinite length helical vortex line at any point $(K, 0, 0)$ on the axis

$$v_x = \frac{\Gamma}{h} F\left(\frac{K}{R}\right) = \frac{\Gamma}{h}\frac{1}{2}\left(1 + \left(1 + \left(\frac{R}{K}\right)^2\right)^{-\frac{1}{2}}\right). \tag{16}$$

Compared to Eq.5, there is an extra factor $F\left(K/R\right)$ in the formula above.

On the other hand, Eq.6 also expresses the unidirectional sequence of vortex rings, if the value range of n is changed to $n = 0, 1, \cdots, +\infty$. At the same time, note that the value range of the parameter ε should expand to $[0, 1]$, considering the disappearance of the symmetry. According to the Biot-Savart Law, it is easy to get the axial induced velocity $v_{S,x}$ of the sequence at $(K, 0, 0)$

$$v_{S,x} = \frac{\Gamma_S}{2R}\sum_{n=0}^{+\infty}\left(1 + (n+\varepsilon)^2\left(\frac{h_S}{R}\right)^2 - 2\frac{K}{R}(n+\varepsilon)\frac{h_S}{R} + \left(\frac{K}{R}\right)^2\right)^{-\frac{3}{2}}. \tag{17}$$

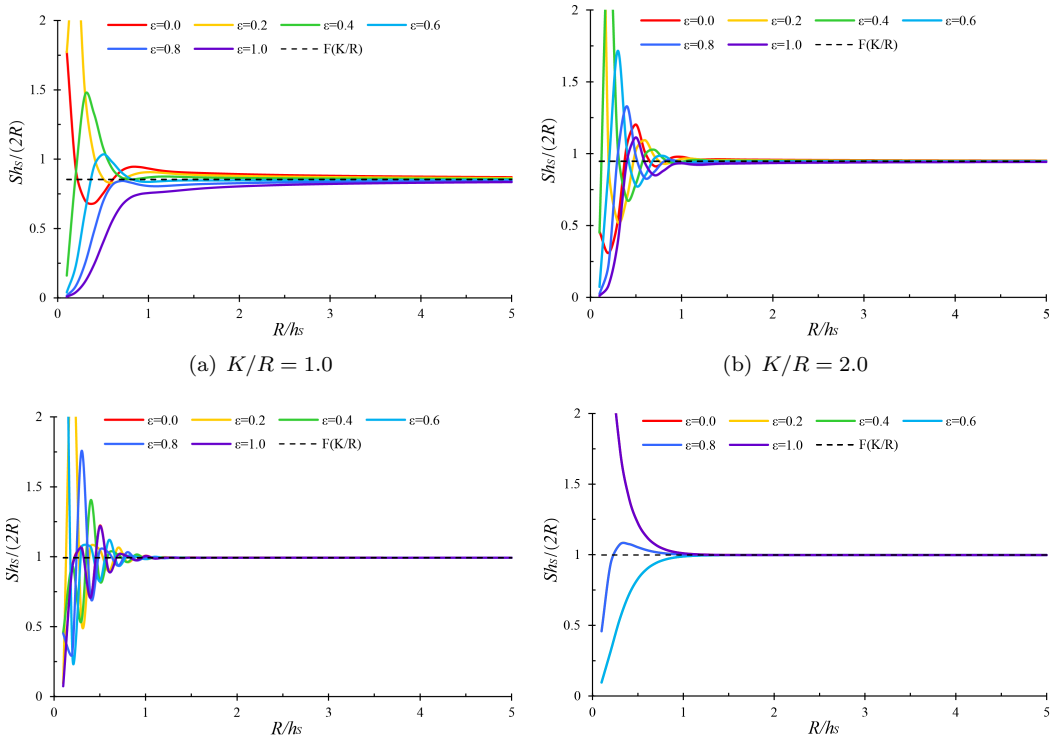

(a) $K/R = 1.0$ (b) $K/R = 2.0$

(c) $K/R = 6.0$ (d) $K/R = 10.0$

Figure 6: The relationship between $Sh_S/(2R)$ and R/h_S when the values of K/R and ε change.

Similarly, the accumulation part of infinite series is S

$$S = \sum_{n=0}^{+\infty} \left(1 + \frac{h_S^2}{R^2} (n+\varepsilon)^2 - 2\frac{h_S}{R}\frac{K}{R} (n+\varepsilon) + \left(\frac{K}{R}\right)^2 \right)^{-\frac{3}{2}}. \tag{18}$$

Inspired by the previous work, consider the value changes of $Sh_S/(2R)$ with R/h_S when the values of K/R and ε vary, and make comparison with $F(K/R)$ in Eq.16. The numerical results are shown in Fig.6. There are four situations where $K/R = 1, 2, 6, 10$ ($K = 0.5D, 1D, 3D, 5D$) respectively. In all these situations, $Sh_S/(2R)$ tends to a fixed value $F(K/R)$ with the increase of R/h_S. It means when the value of R/h_S is big enough, v_x and $v_{S,x}$ have the same form. At this moment, letting $v_x = v_{S,x}$, we can draw the same conclusion as Eq.14. As shown in Fig.6, in the regin of concern ($K/R \geq 2$, i.e., $K/D \geq 1$), the constraint of R/h_S is

$$\frac{h_S}{R} \leq 1. \tag{19}$$

Note that Eq.19 is the same as Eq.11, which means the constraints of Eq.11 and Eq.14 can guarantee that the sequence well approximates the axis induced velocity in the region of concern. At last, there is an interesting numerical phenomenon: as shown in Fig.6(d), when $K/R = 10$, the curves of $Sh_S/(2R)$ coincide with each other under the situations of $\varepsilon = 0.0$ and $\varepsilon = 1.0$, $\varepsilon = 0.2$ and $\varepsilon = 0.8$, $\varepsilon = 0.4$ and $\varepsilon = 0.6$. These coincident curves are the same as the corresponding ones in Fig.5. This is because $K/R = 10 (K = 5D)$ is big enough and this condition is close to the infinite far region where the symmetry shown in Eq.10 comes into

play.

Now, return to the original problem. Assume that the helical vortex line and the vortex ring sequence are released by a vortex line generator and a vortex ring generator respectively in the uniform and stable background flow. The rotation period of the rotor is T and the releasing time interval of the vortex ring generator is T_S, ignoring the interaction between vortices,

$$h = TV_0, \tag{20}$$

$$h_S = T_S V_0, \tag{21}$$

where V_0 is the velocity of the background flow. Combining Eq.11 and Eq.14, get the constraints of the vortex ring generator

$$T_S \leq \frac{R}{V_0}, \tag{22}$$

$$\Gamma_S = \frac{T_S}{T}\Gamma. \tag{23}$$

Take the equal sign in Eq.22, then the parameter configuration of the vortex ring generator is

$$T_S = \frac{R}{V_0}, \tag{24}$$

$$\Gamma_S = \frac{R\Gamma}{V_0 T}, \tag{25}$$

where V_0 is the inflow velocity, T is the rotation period of the rotor, Γ and R are the circulation and the radial shedding position of the tip vortex or the root vortex. If the wind turbine has B blades, we can multiply the right end of Eq.25 by B or multiply the left end of Eq.24 by B.

It is easily seen that the vortex ring releasing time interval in Eq.24 is different for the tip vortex and the root vortex. The releasing of the root vortex is more frequent.

Finally, the constraints of the vortex ring generator(Eq.22 and Eq.23) are necessary considering the process of constructing them, but their justification have not been proved in theory. The validity of the model should be judged by numerical practices.

2.3. The Comparison with the Eulerian Actuator Model

The Lagrangian and Eulerian actuator models both represent the disturbance of the wind turbine rotor to the flow field based on the BEM theory under their respective frameworks to improve the computation efficiency. The physical phenomena corresponding to them are similar. They both treat an actual wind turbine rotor as a virtual and simple geometric structure (a disc or a line), however, they have different expressions, as shown in Fig.7. Compared to the form under the Eulerian framework, the actuator under the Lagrangian framework can affect the fluid just on the margin of the "line" or the "disc". Apparently, the

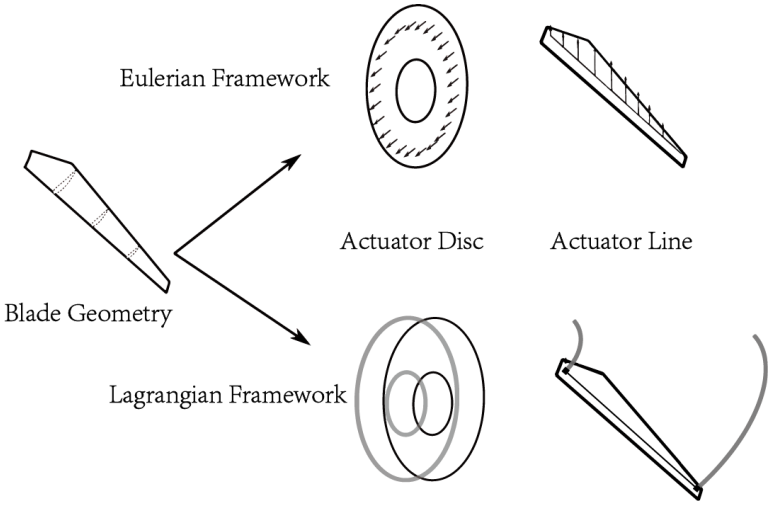

Figure 7: Actuator model under the Eulerian and Lagrangian framework.

dimension reduction helps to improve the computation efficiency, and the vorticity concentration characteristic of the wind turbine wake field provides a fact basis for the LAM.

3. Numerical Method

The Lagrangian actuator model and the vortex method under the Lagrangian framework coordinate well with each other. Numerical simulations and experiments have both suggested that there is apparently intensive vorticities in a wind turbine wake. As to the flow field with intensive vorticities, the vortex method under the Lagrangian framework can give the fullest play to its advantages. The sole problem is that it is difficult to handle the boundary condition on the wind turbine rotor, and the Lagrangian actuator model can remedy it exactly.

According to the geometric feature of discrete elements, the vortex method can be divided into the vortex particle method [33], the vortex filament method [34], the vortex sheet method [35] and the vortex volume method [36]. As for the wake issue of wind turbines, the vortex filament is closer to the vortex structure in an actual wake intuitively. For that reason, this paper chooses the vortex filament as the discrete element, hoping a good balance between computation precision and efficiency.

A wind turbine wake prediction method using the LAL model and the vortex filament element was introduced in authors' previous article where it was called the VFWM [31]. This work will discuss a numerical method based on the LAD model. Similar to the VFWM, this method with obviously higher computation efficiency is deeply inspired by the Pseudo-Implicit Predictor-Corrector (PIPC) method of helicopter aerodynamics [37].

3.1. Vortex Ring

A vortex ring is a round vortex filament end to end as shown in Fig.8, where Γ is the vortex ring circulation, r_c is the vortex core radius, r_h is the vortex ring radius and $O(x, y, z)$ is the central point. In the stable background flow field, if the wind turbine rotor is treated as a vortex ring generator, the velocity field inducted

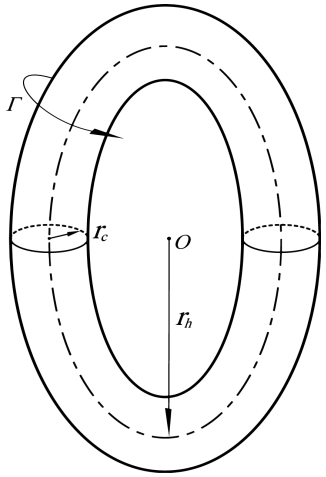

Figure 8: A vortex ring.

by the vortex ring sequence in the wake must be symmetrical to the central line. This means the vortex rings can only move along the central line or rotate around the central line or stretch evenly in this velocity field, but it can not offset, slant or twist. This feature guarantees the reasonableness of using the vortex ring as the basic unit. A vortex ring in the wake can be completely expressed by four parameters, the vortex ring circulation Γ, the vortex core radius r_c, the vortex ring radius r_h and the central axial position x.

The control equation is the N-S equation (the vorticity transport equation)

$$\frac{\partial \boldsymbol{\omega}}{\partial t} = -(\boldsymbol{V} \cdot \nabla)\boldsymbol{\omega} + (\boldsymbol{\omega} \cdot \nabla)\boldsymbol{V} + \nu\Delta \cdot \boldsymbol{\omega}, \tag{26}$$

where ω is the vorticity, V is the velocity and ν is the coefficient of kinematic viscosity. Three on the right hand side represent the convection, stretching and diffusion of vorticity respectively.

The induced velocity of a vortex ring can be calculated through discretizing the ring into some linear vortex filaments and accumulating their induced velocities.

Under the velocity gradient, the vortex ring radius can be stretched to $r_h + \Delta r_h$. At this moment, the vortex core radius will have a corresponding change. Suppose the fluid is incompressible, using the mass conservation law, then the stretching effect on the core radius can be written as

$$2\pi^2 r_c^2 r_h = 2\pi^2 \left(r_c - \Delta r_c\right)^2 \left(r_h + \Delta r_h\right). \tag{27}$$

Then

$$\frac{\Delta r_c}{r_c} = 1 - \sqrt{\frac{r_h}{r_h + \Delta r_h}}. \tag{28}$$

The vortex core growth under the viscosity and turbulent effects can be described by following equations [31].

$$\frac{\mathrm{d}}{\mathrm{d}t} r_c^2 = 4\alpha(\nu + a_1\Gamma + \nu_t), \tag{29}$$

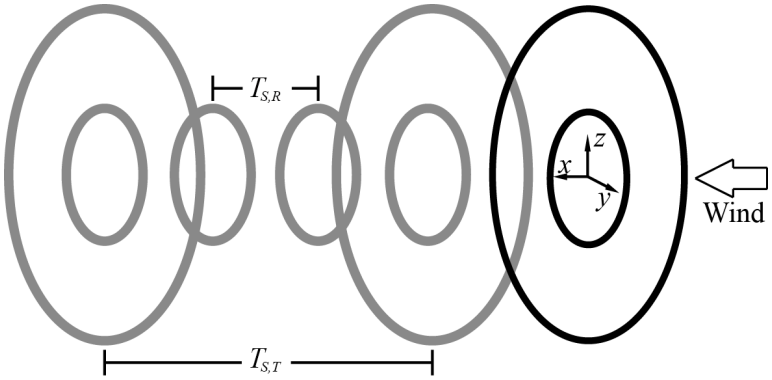

Figure 9: Vortex system from a vortex ring generator.

$$\nu_t = \sqrt{\frac{2}{3}} \frac{A}{\pi K_0^{1.5}} \sqrt{k} \Delta, \tag{30}$$

$$k = \Delta k + k_0, \tag{31}$$

$$\Delta k = min(0.506 V_0^2 a^{1.665} I_0^{0.065} (\frac{x}{D})^{-0.64}, 0.506 V_0^2 a^2), \tag{32}$$

$$a = 0.5(1 - \sqrt{1 - C_T}), \tag{33}$$

where $\alpha = 1.2564$, $a_1 = 5.0 * 10^{-4}$, $K_0 = 1.4$, $A = 0.438$, V_0 is the inflow velocity, I_0 is the inflow turbulence intensity, C_T is the thrust coefficient.

3.2. Numerical Method

The vortex system from a vortex ring generator in the wake is shown in Fig.9. Let $T_{S,T}$ and $\Gamma_{S,T}$ denote the time interval and circulation of the tip vortex rings respectively, $T_{S,R}$ and $\Gamma_{S,R}$ denote those of root vortex rings respectively. Because the constraint in Eq.22 is arbitrary, there are always appropriate $T_{S,T}$ and $T_{S,R}$, satisfying $T_{S,T} = NT_{S,R}$, where N is positive integer. Now, the periodicity in the system is canstructed.

Like the signifying way used in reference [37], a vortex ring in the wake vortex system can be marked by a set of ternary marks (I, η, ξ), among which I has only two values, I_T and I_R, for marking the tip vortex ring and the root vortex ring respectively, ξ denotes the vortex ring life span (from the release time to present time), η denotes the phase time (the elapsed time in the present period). The ring radius r_h, the core radius r_c of the vortex ring and the coordinate x of the central point can all be treated as functions of (I, η, ξ). For a vortex ring, the differential equations of x and r_h are

$$\frac{\mathrm{d}}{\mathrm{d}t} x = V_0 + V_{ind,x}, \tag{34}$$

$$\frac{\mathrm{d}}{\mathrm{d}t}r_h = V_{ind,r}, \tag{35}$$

where $V_{ind,x}$ denotes the axial component of the induced velocity at a certain point, $V_{ind,r}$ denotes its radial component.

Let $x_{i,l,k}$ denote the central point axial coordinate $x(I_i, \eta_l, \xi_k)$ of the vortex ring (I_i, η_l, ξ_k) in simplified form and $r_{hi,l,k}$ denote the ring radius $r_h(I_i, \eta_l, \xi_k)$. Owing to the symmetry, we might as well utilize the flow velocity at the point $(x_{i,l,k}, r_{hi,l,k}, 0)$ on the vortex ring (I_i, η_l, ξ_k) to compute the translation and stretching effects under the flow field. Let $V_{ind,x}\left(x_{i,j,k}, r_{hi,l,k}\right)$ denote the axial component of this velocity and $V_{ind,r}(x_{i,j,k}, r_{hi,l,k})$ denote the radial component. Imitating the PIPC method, a steady solution to the formula above can be constructed:

$$\begin{aligned} x^n_{i,l,k} = x^n_{i,l-1,k-1} + \Delta t[V_0 + \frac{1}{4}(\hat{V}_{ind,x}(x_{i,l,k}, r_{hi,l,k}) + \\ \hat{V}_{ind,x}(x_{i,l,k-1}, r_{hi,l,k-1}) + \hat{V}_{ind,x}(x_{i,l-1,k}, r_{hi,l-1,k}) + \\ \hat{V}_{ind,x}(x_{i,l-1,k-1}, r_{hi,l-1,k-1}))], \end{aligned} \tag{36}$$

$$\begin{aligned} {r_h}^n_{i,l,k} = {r_h}^n_{i,l-1,k-1} + \frac{1}{4}\Delta t(\hat{V}_{ind,r}(x_{i,l,k}, r_{hi,l,k}) + \\ \hat{V}_{ind,r}(x_{i,l,k-1}, r_{hi,l,k-1}) + \hat{V}_{ind,r}(x_{i,l-1,k}, r_{hi,l-1,k}) + \\ \hat{V}_{ind,r}(x_{i,l-1,k-1}, r_{hi,l-1,k-1})), \end{aligned} \tag{37}$$

$$\hat{V}_{ind,x}(x_{i,l,k}, r_{hi,l,k}) = \epsilon V_{ind,x}(x^{n-1}_{i,l,k}, {r_h}^{n-1}_{i,l,k}) + (1-\epsilon)V_{ind,x}(\widetilde{x}_{i,l,k}, \widetilde{r}_{hi,l,k}), \tag{38}$$

$$\hat{V}_{ind,r}(x_{i,l,k}, r_{hi,l,k}) = \epsilon V_{ind,r}(x^{n-1}_{i,l,k}, {r_h}^{n-1}_{i,l,k}) + (1-\epsilon)V_{ind,r}(\widetilde{x}_{i,l,k}, \widetilde{r}_{hi,l,k}), \tag{39}$$

$$\begin{aligned} \widetilde{x}_{i,l,k} = \widetilde{x}_{i,l-1,k-1} + \Delta t[V_0 + \frac{1}{4}(V_{ind,x}(x^{n-1}_{i,l,k}, {r_h}^{n-1}_{i,l,k}) + \\ V_{ind,x}(x^{n-1}_{i,l,k-1}, {r_h}^{n-1}_{i,l,k-1}) + V_{ind,x}(x^{n-1}_{i,l-1,k}, {r_h}^{n-1}_{i,l-1,k}) + \\ V_{ind,x}(x^{n-1}_{i,l-1,k-1}, {r_h}^{n-1}_{i,l-1,k-1}))], \end{aligned} \tag{40}$$

$$\begin{aligned} \widetilde{r}_{hi,l,k} = \widetilde{r}_{hi,l-1,k-1} + \frac{1}{4}\Delta t(V_{ind,r}(x^{n-1}_{i,l,k}, {r_h}^{n-1}_{i,l,k}) + \\ V_{ind,r}(x^{n-1}_{i,l,k-1}, {r_h}^{n-1}_{i,l,k-1}) + V_{ind,r}(x^{n-1}_{i,l-1,k}, {r_h}^{n-1}_{i,l-1,k}) + \\ V_{ind,r}(x^{n-1}_{i,l-1,k-1}, {r_h}^{n-1}_{i,l-1,k-1})), \end{aligned} \tag{41}$$

where ϵ is the relaxing factor. The core radius r_c in the iteration can be calculated as stated in section 3.1.

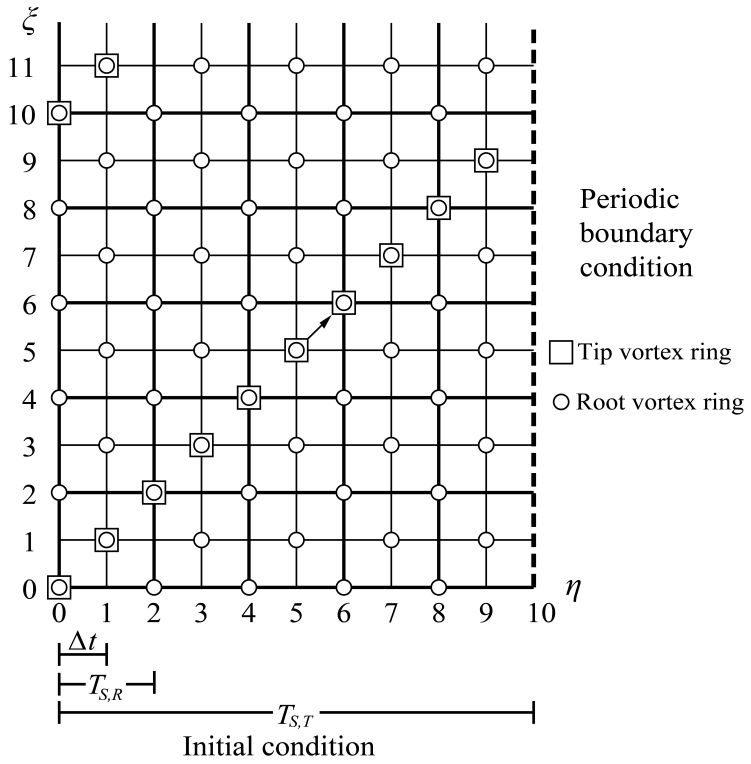

Figure 10: The discretization and iteration in computational domain.

The initial condition is

$$x(I, \eta, 0) = 0, \tag{42}$$

$$r_h(I, \eta, 0) = r_{h,shed}(I), \tag{43}$$

$$r_c(I, \eta, 0) = r_{c,shed}(I). \tag{44}$$

In these equations, $r_{h,shed}(I)$ is the initial radius of the tip vortex or the root vortex which can be calculated through BEM theory. $r_{c,shed}(I)$ is the initial core radius of the tip vortex or the root vortex which is usually 10% of the average chord length of the blade and the numerical result is not sensitive to the value.

Owing to the inherent periodicity, the wake vortex system will return to the former condition after $T_{S,T}$, then the natural periodic boundary condition is

$$x\,(I, \eta, \xi) = x(I, \eta + T_{S,T}, \xi), \tag{45}$$

$$r_h\,(I, \eta, \xi) = r_h(I, \eta + T_{S,T}, \xi). \tag{46}$$

The discretisation and initial condition and periodic boundary condition of the whole computational domain are shown in Fig.10. For convenience in the signification, we make $T_{S,T} = 5T_{S,R} = 10\Delta t$.

The sequence of vortex rings with equal distance can be used to initiate the first iteration. Iteration convergence can be identified through the formula below

$$RMS = \frac{1}{i_{max} l_{max} k_{max} D} \sqrt{\sum_i \sum_l \sum_k (\left| x_{i,l,k}^n - x_{i,l,k}^{n-1} \right|^2 + \left| r_{h_{i,l,k}}^n - r_{h_{i,l,k}}^{n-1} \right|^2)}, \tag{47}$$

where D is the wind turbine rotor diameter. When RMS is smaller than a certain threshold value, it can be treated as computation convergence.

4. Verification

The LAD model is verified through a wind tunnel test. The detailed information of this test including the specific parameters, aerodynamic performance and wake characteristics, can be found in references [38, 39]. The test wind turbine is a two-bladed upwind HAWT with a rotor diameter of $D = 0.5m$. Three cases with the same free-stream velocity $7m/s$ and different ambient turbulence intensities (TI) of 1.4%, 8.0% and 13.5% are tested at the optimum tip speed ratios respectively.

In numerical simulations, $T_{S,T} = 6T_{S,R} = 18\Delta t = 0.0342s$. The convergent identification threshold value is set to be 0.1%. The numerical results and comparison among experimental measurement data are shown in Fig.11.

In addition, a comparison between the present results, the Jensen model [7] and the improved Jensen model [12] is put forward. When TI=8%, the comparison of these two models with the test data and with the LAD model is shown in Fig.12.

The computation result of the numerical method above is almost the same as that of the numerical method VFWM using the LAL model in reference [31]. However, in terms of computation speed, using a quad core i5 processor, the parallel running time of the VFWM is about 30 minutes, and that of the numerical method based on the LAD model is less than 30 seconds.

5. Wake Characteristics

It has been shown that the new numerical method constructed with the Lagrangian actuator model and the vortex method is simple and efficient. It works in the whole wake, which indicates that the description of the wind turbine wakes from the perspective of vorticity is effective and universal. It is unnecessary to artificially divide the wake field into the near wake and the far wake and try to find the boundary between them. Based on it, this work will build the vorticity description framework of the wind turbine wakes.

5.1. Geometric characteristic Parameters of the Vortex System

Under the LAL model, three parameters, the core radius $r_{c,LAL}$, the helix radius $r_{h,LAL}$ and the local pitch P_{LAL}, can be used to characterize the helix-like vortex lines in a wake. Let $x_{LAL}(I, \psi, \zeta)$, $y_{LAL}(I, \psi, \zeta)$ and $z_{LAL}(I, \psi, \zeta)$ denote three components of the position of a collection point (I, ψ, ζ) at the rectangular coordinate system $oxyz$, $r_{c,LAL}(I, \psi, \zeta)$ denote the core radius, and $\Gamma(I_T) = -\Gamma(I_R)$ denote vortex circulation. In these

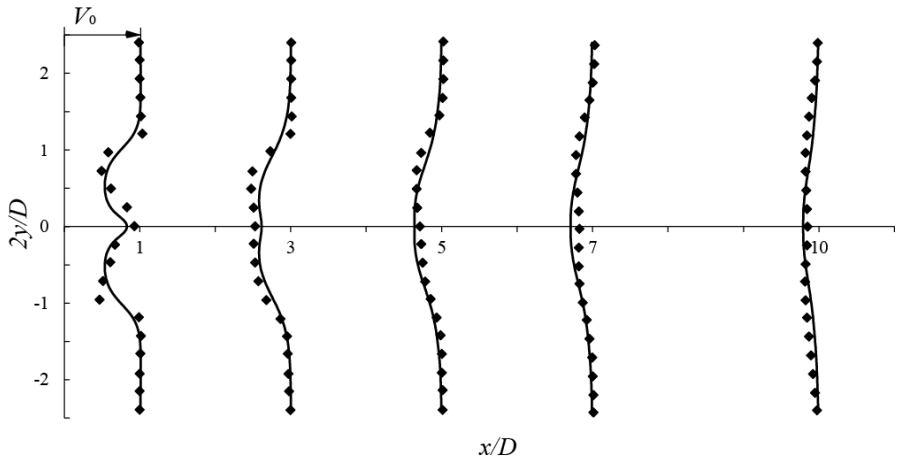

(a) TI=1.4%

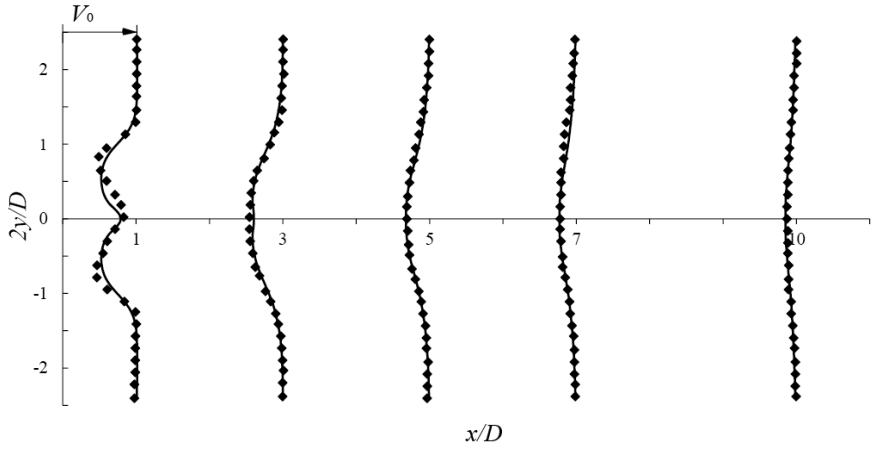

(b) TI=8.0%

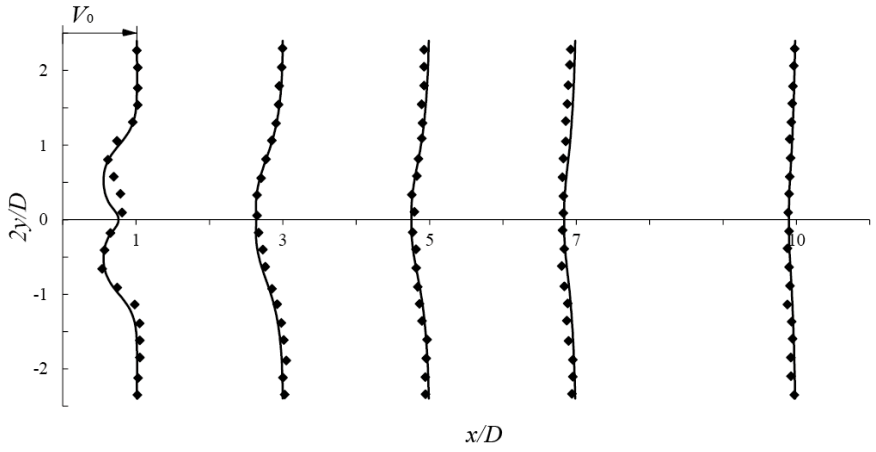

(c) TI=13.5%

Figure 11: Comparison between measurements and simulations using the LAD model.

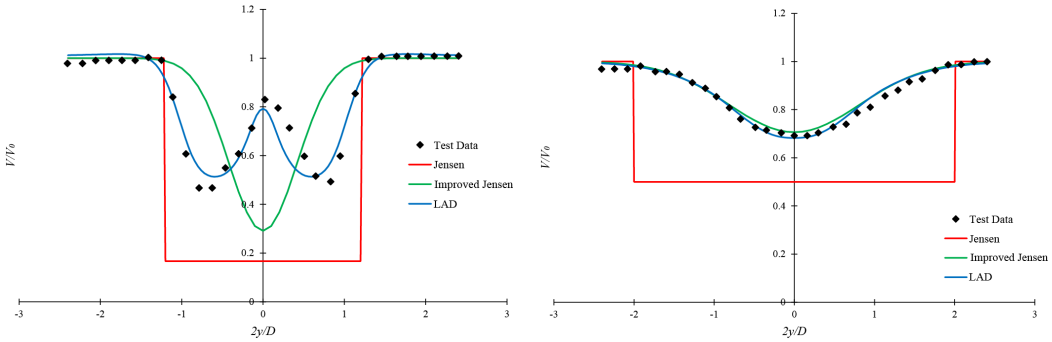

(a) $x = 1D$ (b) $x = 5D$

Figure 12: Comparison with the Jensen wake model and the improved Jensen wake model.

significations, I is the mark that distinguishes the tip vortex (I_T) and the root vortex (I_R); ψ denotes phase angle; ζ denotes life angle (see reference [31] for detailed information). Define the local helix radius $r_{h,LAL}$ at the configuration point (I, ψ, ζ)

$$r_{h,LAL} = \sqrt{y_{LAL}^2(I,\psi,\zeta) + z_{LAL}^2(I,\psi,\zeta)}, \tag{48}$$

and the local pitch P_{LAL}

$$P_{LAL} = 2\pi \frac{\mathrm{d}}{\mathrm{d}\zeta} x_{LAL}(I,\psi,\zeta). \tag{49}$$

Their non-dimension forms are

$$\overline{r}_{h,LAL} = \frac{2}{D}\sqrt{y_{LAL}^2(I,\psi,\zeta) + z_{LAL}^2(I,\psi,\zeta)}, \tag{50}$$

$$\overline{P}_{LAL} = \frac{2\pi}{D}\frac{\mathrm{d}}{\mathrm{d}\zeta} x_{LAL}(I,\psi,\zeta), \tag{51}$$

$$\overline{r}_{c,LAL} = \frac{2r_{c,LAL}}{D}. \tag{52}$$

Similarly, under the LAD model, the characteristic parameters of the vortex ring sequences in wakes are the ring radius $r_{h,LAD}$, the core radius $r_{c,LAD}$ and the local pitch P_{LAD}. Their non-dimension forms can be defined as

$$\overline{r}_{h,LAD} = \frac{2r_{h,LAD}}{D}, \tag{53}$$

$$\overline{P}_{LAD} = \frac{T}{D}\frac{\mathrm{d}}{\mathrm{d}\xi} x_{LAD}(I,\eta,\xi), \tag{54}$$

$$\overline{r}_{c,LAD} = \frac{2r_{c,LAD}}{D}, \tag{55}$$

where T is the rotating period of the wind turbine rotor.

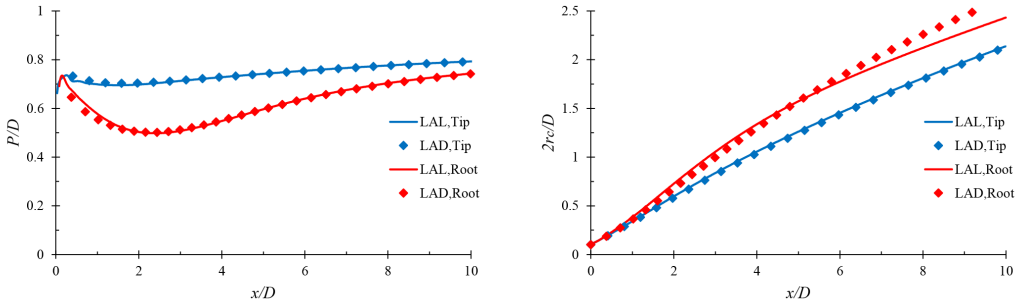

(a) P/D (b) $2r_c/D$

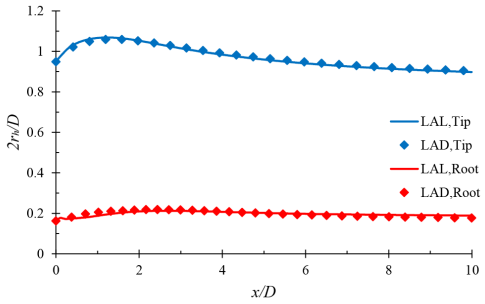

(c) $2r_h/D$

Figure 13: Geometric characteristics Parameters under the LAL and the LAD model.

5.2. Wake Characteristics

The changing curves of parameters expressed in Eq.50 $\sim$ Eq.55 with the non-dimension downstream distance x/D when TI=8% are shown in Fig13. It is easy to see that the vortex systems achieved through the LAL model and the LAD model behave almost the same in terms of those geometric characteristics.

Helix radiuses (ring radiuses) of the tip and root vortices remain largely unchanged along the downstream distance. Local pitches of the tip and root vortices change little relatively along the downstream distance and they gradually tend to be the same value

$$\overline{P}_{\infty} = \frac{TV_0}{D}. \tag{56}$$

Different to the helix radius (or the ring radius) and the local pitch, the core radius of the tip vortex or the root vortex rapidly increases along the downstream distance. For that reason, it is easily seen that the vortex core growth, which is mainly controlled by turbulence, is the most important factor of the wake evolution.

As for the way in which core radius influences the wake velocity deficit, see the example below. First, define a dimensionless coefficient, the radius ratio

$$a = \frac{r_c}{r_h}. \tag{57}$$

which represents the ratio of the core radius to the helix radius(or the ring radius). Then, compare the induced velocity profiles of infinite vortex ring sequences (helical vortex lines) with different radius ratios ($a = 0.5, 1.0, 1.5, 2.0, 3.0$) on appropriate cross sections. The results are shown in Fig.14. The horizontal axis

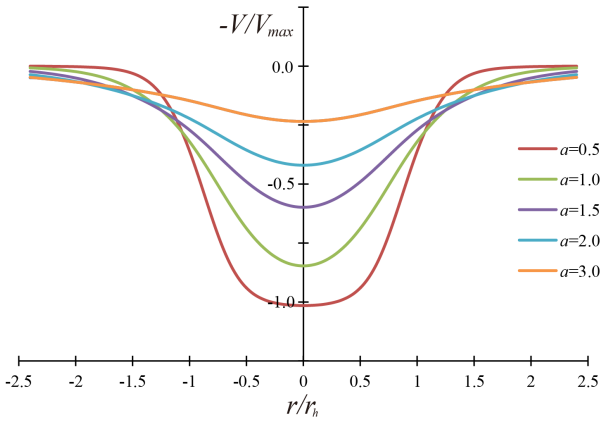

Figure 14: Comparison of induced velocity profiles of vortex ring sequences with different radius ratios.

represents the non-dimensional distance r/r_h, and the vertical axis represents the non-dimensional induced velocity V/V_{max}, where $V_{max} = \Gamma/h$ is the induced velocity when $a = 0$ given by Eq.5. As can been seen, the induced velocity profile of the vortex ring sequence with $a = 0.5$ is in the shape of a top-hat. With the increase of the radius ratio, the highest induced velocity gradually decreases and the profile curve tends to be moderate, being in the shape of a Gaussian function.

Up to now, we can describe the evolution of the velocity deficit in wakes from the perspective of the vortex system. The vortices released from the blade tip and root form two sets of vortex ring sequences (helical vortex lines) with different ring radius (helix radius) in the wake, which are called the tip vortex and the root vortex respectively. They have circulations with the same absolute value but different directions: the direction of the induced velocity of the tip vortex is opposite to that of the inflow to cause the velocity deficit, while the induced velocity of the root vortex tries to recover the inflow velocity. When the cores of the tip and root vortices have not fully grown near the wind turbine rotor, the induced velocity fields superpose with each other, forming the M-shape profile. With the development of the wake along the downstream distance, the core radius of the tip and root vortices swell in the similar velocity under the diffusion effect of turbulence. But the influence of the root vortex on the velocity field is weakened faster owing to its lower radius ratio. Therefore, in the farther wake, the velocity deficit is mainly controlled by the tip vortex, forming the velocity profile in the shape of a Gaussian function and gradually tends to become moderate until it totally recovers.

5.3. Similarity of Wakes

At present, most detailed experiments of wind turbine wakes are tested in wind tunnels. The rotor diameter of a modern large wind turbine can reach more than 100 meters, but the rotor diameter of a small wind turbine used in experiments is usually less than several metres. Naturally, there is a question as follows: Can a wind tunnel experiment using a small wind turbine reflect the actual wake field of a full-scale wind turbine? In other words, is there similarity in wake field between two wind turbines with huge size difference? Which similarity criterion is connected with this similarity? These questions are easily to be answered in the vortex framework[31]. We provide the conclusion directly here: 1) under the general inflow condition and operational state, the wind turbines with different sizes have similar wakes; 2) the power coefficient of the wind turbine

and the inflow turbulence intensity are similarity criteria for measuring the similarity. Note that the similarity of wind turbine wakes contains almost no scale effect. This conclusion provides a more flexible and broad scale range for the design of wind tunnel tests.

6. Conclusion

Coordinating with the vortex method, the Lagrangian actuator model proposed in this paper can be used for the wind turbine wake prediction with good accuracy and efficiency. It is noteworthy that the novel method works in the whole wake, not just in the far wake.

Based on that, a vorticity description framework for wind turbine wakes centered on vortex geometric structures is established. Under the framework, wake phenomenon can be described in a simple and universal way, thus avoiding the vague definition of the near wake and the far wake. Moreover, it provides an approach to analyze complex velocity field in a wind turbine wake, and the main conclusions are drawn as follows: 1) the wake deficit is deeply influenced by the vortex system evolution, especially the vortex core growth which is mainly controlled by turbulence; 2) It is hard and unnecessary to draw a clear line of demarcation between the near wake and the far wake because there are no obvious distinctions between their physical mechanisms; 3) Similarity exist between wakes of wind turbines with size difference, and the power coefficient and the inflow turbulence intensity are similarity criteria.

Acknowledgements

This work is supported by the basic research and cutting-edge technology projects of State Administration of Science (No. JCKY2019604C003).

References

[1] Park J, Law KH. Layout optimization for maximizing wind farm power production using sequential convex programming. Applied Energy 2015;151(151):320–34.

[2] Barthelmie RJ, Pryor SC. An overview of data for wake model evaluation in the virtual wakes laboratory. Applied Energy 2013;104:834–44.

[3] Gao X, Yang H, Lu L. Optimization of wind turbine layout position in a wind farm using a newly-developed two-dimensional wake model. Applied Energy 2016;174:192–200.

[4] Vermeer LJ, Sorensen JN, Crespo A. Wind turbine wake aerodynamics. Progress in Aerospace Sciences 2003;39(6):467–510.

[5] Mo J, Choudhry A, Arjomandi M, Lee Y. Large eddy simulation of the wind turbine wake characteristics in the numerical wind tunnel model. Journal of Wind Engineering and Industrial Aerodynamics 2013;112:11–24.

[6] Larsen GC, Madsen Aagaard H, Bingöl F, Mann J, Ott S, Sørensen JN, et al. Dynamic wake meandering modeling. Tech. Rep.; Risø National Laboratory; 2007.

[7] Jensen NO. A note on wind turbine interaction. Tech. Rep.; Risø National Laboratory; 1983.

[8] Barthelmie RJ, Larsen GC, Frandsen ST, Folkerts L, Rados K, Pryor SC, et al. Comparison of wake model simulations with offshore wind turbine wake profiles measured by sodar. Journal of Atmospheric and Oceanic Technology 2006;23(7):888–901.

[9] Chamorro LP, Porteagel F. A wind-tunnel investigation of wind-turbine wakes: Boundary-layer turbulence effects. Boundary-Layer Meteorology 2009;132(1):129–49.

[10] Gaumond M, Rethore P, Ott S, Pena A, Bechmann A, Hansen KS. Evaluation of the wind direction uncertainty and its impact on wake modeling at the horns rev offshore wind farm. Wind Energy 2014;17(8):1169–78.

[11] Bastankhah M, Porteagel F. A new analytical model for wind-turbine wakes. Renewable Energy 2014;70:116–23.

[12] Ishihara T, Qian G. A new gaussian-based analytical wake model for wind turbines considering ambient turbulence intensities and thrust coefficient effects. Journal of Wind Engineering and Industrial Aerodynamics 2018;177:275–92.

[13] Sun H, Yang H. Study on an innovative three-dimensional wind turbine wake model. Applied Energy 2018;226:483–93.

[14] Gao X, Li B, Wang T, Sun H, Yang H, Zhao F. Investigation and validation of 3d wake model for horizontal-axis wind turbines based on filed measurements. Applied Energy 2020;260:114272.

[15] Sun H, Yang H. Numerical investigation of the average wind speed of a single wind turbine and development of a novel three-dimensional multiple wind turbine wake model. Renewable Energy 2020;147:192–203.

[16] Keane A, Aguirre PEO, Ferchland H, Clive P, Gallacher D. An analytical model for a full wind turbine wake. Journal of Physics Conference 2016;753(3):032039.

[17] Masaru H, Yuji O, Hiroaki K. Numerical studies of flows around a wind turbine equipped with a flanged diffuser shroud by using an actuator-disc model. Journal of Web Engineering 2006;73(108):335–8.

[18] Sedaghatizadeh N, Arjomandi M, Kelso R, Cazzolato B, Ghayesh MH. Modelling of wind turbine wake using large eddy simulation. Renewable Energy 2018;115:1166–76.

[19] Uchida T, Yoshida T, Inui M, Taniyama Y. Doppler lidar investigations of wind turbine near-wakes and les modeling with new porous disc approach. Energies 2021;14(8):2101.

[20] Abdelsalam AM, Boopathi K, Gomathinayagam S, Kumar SSHK, Ramalingam V. Experimental and numerical studies on the wake behavior of a horizontal axis wind turbine. Journal of Wind Engineering and Industrial Aerodynamics 2014;128:54–65.

[21] Sanderse B, Pijl VDS, Koren B. Review of computational fluid dynamics for wind turbine wake aerodynamics. Wind Energy 2011;14(7):799–819.

[22] Kuo J, Rehman D, Romero DA, Amon CH. A novel wake model for wind farm design on complex terrains. Journal of Wind Engineering and Industrial Aerodynamics 2018;174:94–102.

[23] Crespo A, Hernandez J, Frandsen S. Survey of modelling methods for wind turbine wakes and wind farms.

Wind Energy 1999;2(1):1–24.

[24] Ammara I, Leclerc C, Masson C. A viscous three-dimensional differential/actuator-disk method for the aerodynamic analysis of wind farms. Journal of Solar Energy Engineering-transactions of The Asme 2002;124(4):345–56.

[25] Sorensen JN, Shen WZ. Numerical modeling of wind turbine wakes. Journal of Fluids Engineering-transactions of The Asme 2002;124(2):393–9.

[26] Shen WZ, Zhang JH, Sorensen JN. The actuator surface model: A new navier–stokes based model for rotor computations. Journal of Solar Energy Engineering-transactions of The Asme 2009;131(1):011002.

[27] Rajagopalan RG, Klimas PC, Rickerl TL. Aerodynamic interference of vertical axis wind turbines. Journal of Propulsion and Power 1990;6(5):645–53.

[28] Gao ZT, Li Y, Wang TG, Ke ST, Li DS. Recent improvements of actuator line-large-eddy simulation method for wind turbine wakes. Applied Mathematics and Mechanics 2021;42(4):1–16.

[29] Adedipe TA, Chaudhari A, Kauranne T. Impact of different forest densities on atmospheric boundary-layer development and wind-turbine wake. Wind Energy 2020;23(5):1165–80.

[30] Meng H, Li L, Zhang J. A preliminary numerical study of the wake effects on the fatigue load for wind farm based on elastic actuator line model. Renewable Energy 2020;162:788–801.

[31] Liu W, Liu W, Zhang L, Sheng Q, Zhou B. A numerical model for wind turbine wakes based on the vortex filament method. Energy 2018;157:561–70.

[32] Dasari T, Wu Y, Liu Y, Hong J. Near-wake behaviour of a utility-scale wind turbine. Journal of Fluid Mechanics 2019;859:204–46.

[33] Beale JT, Majda AJ. Vortex methods. i. convergence in three dimensions. Mathematics of Computation 1982;39(159):1–27.

[34] Leonard A. Computing three-dimensional incompressible flows with vortex elements. Annual Review of Fluid Mechanics 1985;17(1):523–59.

[35] Brady M, Leonard A, Pullin DI. Regularized vortex sheet evolution in three dimensions. Journal of Computational Physics 1998;146(2):520–45.

[36] Carley M. A triangulated vortex method for the axisymmetric euler equations. Journal of Computational Physics 2002;180(2):616–41.

[37] Bagai A, Leishman JG. Rotor free-wake modeling using a pseudo-implicit technique—including comparisons with experimental data. Journal of the American Helicopter Society 1995;40(3):29–41.

[38] Li Q, Murata J, Endo M, Maeda T, Kamada Y. Experimental and numerical investigation of the effect of turbulent inflow on a horizontal axis wind turbine (part i: Power performance). Energy 2016;113:713–22.

[39] Li Q, Murata J, Endo M, Maeda T, Kamada Y. Experimental and numerical investigation of the effect of turbulent inflow on a horizontal axis wind turbine (part ii: Wake characteristics). Energy 2016;113:1304–15.